Journal of Applied Physics

RESEARCH ARTICLE | SEPTEMBER 09 2020

{001}-textured $Pb(Zr, Ti)O_3$ thin films on stainless steel by pulsed laser deposition

Juliette Cardoletti ; Philipp Komissinskiy ; Enrico Bruder ; Carl Morandi ; Lambert Alff

J. Appl. Phys. 128, 104103 (2020)
https://doi.org/10.1063/5.0019967

Journal of Applied Physics ARTICLE scitation.org/journal/jap

{001}-textured $Pb(Zr, Ti)O_3$ thin films on stainless steel by pulsed laser deposition

Cite as: J. Appl. Phys. **128**, 104103 (2020); doi: 10.1063/5.0019967
Submitted: 26 June 2020 · Accepted: 25 August 2020 ·
Published Online: 9 September 2020

Juliette Cardoletti,[1,a)] Philipp Komissinskiy,[1] Enrico Bruder,[1] Carl Morandi,[2] and Lambert Alff[1]

AFFILIATIONS

[1]Institute of Materials Science, Technische Universität Darmstadt, Alarich-Weiss-Straße 2, 64287 Darmstadt, Germany
[2]George W. Woodruff School of Mechanical Engineering, Georgia Institute of Technology, 771 Ferst Drive, Atlanta, Georgia 30332, USA

[a)]**Author to whom correspondence should be addressed:** juliette.cardoletti@tu-darmstadt.de

ABSTRACT

In this work, we report nearly single oriented {001}-textured ferroelectric $PbZr_{0.52}Ti_{0.48}O_3$ thin films grown by pulsed laser deposition onto AISI 304 stainless steel substrates. Pt, Al_2O_3, and $LaNiO_3$ buffer layers promote the $PbZr_{0.52}Ti_{0.48}O_3$ {001} texture and protect the substrate against oxidation during deposition. The dominant {001} texture of the $PbZr_{0.52}Ti_{0.48}O_3$ layer was confirmed using x-ray and electron backscatter diffraction. Before poling, the films exhibit a permittivity of about 350 at 1 kHz and a dielectric loss below 5%. The films display a remanent polarization of about $16.5\,\mu C\,cm^{-2}$ and a high coercive field of up to $E_c = 135.9\,kV\,cm^{-1}$. The properties of these $PbZr_{0.52}Ti_{0.48}O_3$ thin films on stainless steel are promising for various MEMS applications such as transducers or energy harvesters.

I. INTRODUCTION

Due to their large piezoelectric coefficient, bulk lead zirconate titanate ceramics have long imposed themselves as the material of choice for transducers, sensors, and actuators. As new challenges emerge, piezoelectric microelectromechanical systems (PiezoMEMS) move toward smaller sizes, increasing the necessity for efficient ferroelectric thin films.[1–3]

The deposition of lead zirconate titanate thin films on various substrates such as Si, Pt-coated Si, glass, or single-crystal perovskite substrates is well established.[1,4–6] However, Si and glass substrates can be brittle and unsuitable for demanding mechanical applications such as actuators or energy harvesters and may induce failure.[7] Therefore, deposition of efficient piezoelectric thin films on metallic substrates is required for industrial applications.

In the literature, the majority of the few pertinent reports is focused on sol-gel procedures on a variety of metallic substrates,[8–11] including the growth of {001}-oriented lead zirconate titanate thin films on Ni foils.[12–14] Several studies report lead zirconate titanate films of various textures grown on stainless steel by the sol-gel method,[15] electrochemical reduction,[16] electron beam evaporation technique,[17] or RF-magnetron sputtering.[18–20] {001}-oriented lead zirconate titanate thin films on steel, reported by Morimoto *et al.*, were grown by RF-magnetron sputtering on Pt/MgO substrates before being glued onto stainless steel with epoxy.[7]

To our best knowledge, however, there are no conclusive reports showing tetragonal {001}-textured lead zirconate films grown directly on stainless steel by physical vapor deposition, such as sputtering or pulsed laser deposition. Yet, engineering of {001} texture is required to improve the piezoelectric response of lead zirconate titanate films.[14]

In this work, we report the growth of {001}-textured ferroelectric $PbZr_{0.52}Ti_{0.48}O_3$ (PZT) thin films using Pulsed Laser Deposition (PLD) on stainless steel 304 substrates covered with Pt, Al_2O_3, and $LaNiO_3$ (LNO) buffer layers with promising ferroelectric properties.

II. EXPERIMENTAL PROCEDURE

Commercially available cold-rolled 0.2 mm thick AISI 304 stainless steel (SS304) was chosen as a substrate material. Pieces of SS304 were diced into $5 \times 5\,mm^2$ substrates using a Microace 3 dicing saw by Loadpoint.

The average roughness of 189 nm and the standard deviation of 236 nm of the as bought SS304 were measured by a Dektak XT profilometer by Bruker. Decreasing the substrate surface roughness promotes the texture of LNO and subsequently of PZT.[12]

Therefore, substrates were polished using a PM5 Precision Lapping & Polishing Machine by Logitech with a slurry of amorphous SiO_2 with a particle size of 32 nm. After polishing, the average roughness and standard deviation were reduced to 3 nm and 4 nm, respectively.

To prevent oxidation during the deposition of the subsequent layers, 30 nm of Pt (Umicore, 99.99%) were sputtered onto the SS304 substrates. Sputtering was performed at room temperature using a Q300T DC magnetron sputter coater by Quorum Technologies with a current of 30 mA in Ar atmosphere at a pressure of 1 Pa.

In the next steps, Al_2O_3 and LNO buffer layers were grown onto the Pt buffer. The LNO layer provides a growth template for PZT and acts as a bottom electrode of the parallel-plate capacitors.[12,21] The 5 nm thick amorphous Al_2O_3 layer is necessary to enable the LNO growth as the surface of the underneath Pt layer is unstable under the LNO deposition conditions described below.

The Al_2O_3 (Kurt J. Lesker, 99.5%) layer was deposited by RF-magnetron sputtering at 40 W in Ar atmosphere at a pressure of 0.64 Pa. The substrate temperature was maintained at 100 °C as measured on the sample holder by a thermocouple.

Thin films of LNO and PZT were grown onto the Al_2O_3/Pt/*SS*304 heterostructure by PLD using custom-made systems.

The LNO PLD target was produced from a stoichiometric mixture of La_2O_3 (Alfa Aesar, 99.99%) and NiO (Chempur, 99.995%). The individual powders were dried at 1000 °C for 12 h and at 400 °C for 1.5 h, respectively, to remove absorbed moisture. The powders were mixed in a stoichiometric ratio, and a slurry was made with isopropyl alcohol (99.99%). The slurry was ball-milled at 500 rpm for 30 min using ZrO_2 milling media. The powder was dried in air before being calcinated at 1100 °C for 20 h. The obtained powder was ball-milled in the same conditions as stated previously and then pressed uniaxially at ∼28 MPa and isostatically at ∼360 MPa. In the last step, the green body was sintered at 1300 °C for 24 h to obtain an LNO target with a density of 96% of the theoretical LNO density.[22] The $PbZr_{0.52}Ti_{0.48}O_3$ target was commercially bought (Testbourne, 99.9%).

The films were deposited using a KrF laser by Coherent with a wavelength of 248 nm. For the growth of LNO and PZT films, the substrate-target distance was fixed at 40 mm and 32 mm, and the repetition rate of the laser was set to 2 Hz and 10 Hz, respectively. The 57 nm thick LNO buffer layer was grown with a fluence of 2 J cm^{-2} under 1.3 Pa of O_2. During the LNO deposition, the substrate temperature of 500 °C was measured by a pyrometer focused on the back side of the sample holder. The PZT layer was deposited with a fluence of 1 J cm^{-2} in oxygen atmosphere at 6.5 Pa. The substrate temperature of 650 °C during the PZT deposition was measured by a thermocouple on the substrate holder. The PZT films were grown with a thickness of 200 nm or 400 nm. The 400 nm thick film was grown to see the influence of possible leakage currents.

In order to fabricate top electrodes, a 30 nm thick platinum layer was grown on the PZT/LNO/Al_2O_3/Pt/SS304 heterostructure, using DC magnetron sputtering, and then patterned, applying a standard photoresist lift-off process. Contact to the LNO bottom electrode was made at a corner of the sample, where the PZT layer was removed using Ar ion milling with a custom-made RF ion source by Meyer Burger. The resulting structure is schematically represented in Fig. 1.

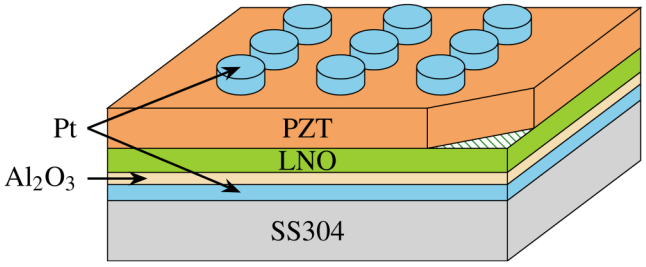

FIG. 1. Schematic representation of the PZT/LNO/Al_2O_3/Pt/steel heterostructure with Pt electrodes on top. The access to the LNO bottom electrode is indicated by the striped pattern. Dimensions are not to scale.

X-ray diffraction (XRD) measurements were performed with monochromatic Cu Kα_1 radiation, using a SmartLab diffractometer by Rigaku equipped with a graphite monochromator and a 2 mm wide horizontal primary slit.

Electron backscatter diffraction (EBSD) was performed using a MIRA3-XMH high resolution scanning electron microscope (SEM) by TESCAN, equipped with a DIGIVIEW 5 EBSD system by EDAX. The system was operated at an acceleration voltage of 15 keV and a beam current of 500 pA to achieve a high spatial resolution. The step size was set to 10 nm, which is below the physical resolution of conventional EBSD, owing to the coarsening effect induced by the NPAR® (Neighbor Pattern Averaging and Reindexing) post-processing routine that was used to improve the data quality without further cleanup procedures. The crystallographic texture was calculated based on an EBSD dataset with more than 7000 indexed grains via the harmonic series expansion method with a series rank of 24, a Gaussian half width of 5°, and no enforced symmetry.

Permittivity measurements were performed using an E4980A LCR meter by Agilent. Polarization vs electric field hysteresis (*P*–*E*) loops were obtained using a TF Analyzer 2000 *P*–*E* loop tracer by aixACCT equipped with a FE module. For both measurements, a probe station equipped with S-725 micropositioners by Signatone, mounted with tungsten tips of 25 μm in diameter, was used. The permittivity and dielectric loss of the PZT films were measured at zero DC bias with an AC driving signal of $V_{AC} = 30$ mV at 1 kHz. The amplitude of the driving signal is lower than half of the coercive field of the thin films. To measure the *P*–*E* loops, a single triangular waveform with a frequency of 100 Hz and a prepulse loop was applied.

DC leakage current measurements were performed using a 4200-SCS Semiconductor Characterization System by Keithley equipped with two 4200-SMU (Source Measure Unit) cards and a 4200-PA preamplifier. The sample was contacted, using a TTPX probe station by Lake Shore, equipped with beryllium-copper tips of 25 μm in diameter. The hold time of 75 s before measuring each data point was used to minimize the contribution of current relaxation effects to the measured value of the leakage current. The bottom electrode was grounded, while the DC bias was applied to the top electrode.

III. RESULTS AND DISCUSSION

In this work, it is observed that the SS304 substrates are flat during the dicing and polishing steps of the experimental

procedure. However, they bend in an U-shape concavely around the PZT-deposited side during the deposition of buffer and PZT layers. The curvature of the sample with a bending radius of a few millimeters, appearing in the steel rolling direction, is sufficiently pronounced to be observable by eye. This bending also occurs when an uncoated substrate goes through thermal treatment equivalent to the successive depositions of buffer and PZT layers. This phenomenon can be attributed to the elongation of the cold-rolled steel during the heating at deposition temperatures.

The industrial processing of stainless steel into thin sheets incorporates cold rolling and coiling/uncoiling procedures that generate residual stresses in the material. The deposition of LNO at 500 °C and PZT at 650 °C represents a stress relief annealing for the SS304 substrate, which can result in warpage in the case of an asymmetric residual stress distribution.

It should be noted that the curvature cannot be explained by thermal strain. Indeed, stainless steel 304 exhibits a thermal expansion coefficient of $16.5 \times 10^{-6}\,K^{-1}$ at 20 °C.[23] This is larger than the thermal expansion coefficient of PZT, ranging from $8 \times 10^{-6}\,K^{-1}$ in the paraelectric phase to $2 \times 10^{-6}\,K^{-1}$ in the ferroelectric phase with a discontinuity at Curie temperature.[14] Therefore, if thermal strain was the driving force of the samples' curvature, samples should be convex on the PZT-deposited side, which is not the case in this work.

The XRD pattern of a PZT thin film is shown in Fig. 2. It should be noted that the LNO reflections and the ones from SS304 and Pt, labelled as "substrate peaks," are observed before the deposition of PZT.

The film shows a perovskite structure with reflections from multiple orientations visible in the XRD pattern, e.g., {001}, {101}, {111}, {102}, and {112}. The orientation is predominantly {001} as the calculated Lotgering factor,[24] f, is $f_{PZT} = 0.91$. It should be noted that during the deposition of PZT, the chromium present in the SS304 substrates forms an intermetallic compound, CrPt, as can be seen in Fig. 2(c). Small $Pb_2Ti_2O_6$ pyrochlore reflections are also visible. Despite the formation of these additional phases, f_{PZT} is larger than the Lotgering factor for the LNO layer acting as a growth template, which is itself {100}-textured, with $f_{LNO} = 0.68$. Note that a similar value of 0.70 of the Lotgering factor has been reported in the literature[15] for LNO films grown using a sol-gel method on stainless steel substrates.

An SEM image of the PZT film surface is presented in Fig. 3. The PZT grain size is ≈45.3 nm with a standard deviation of 4.8 nm as estimated by the intercept method averaged over 30 measurements. It is mostly homogeneous over the SEM image. The grain size obtained from the SEM image is larger than the out-of-plane crystallite size of 30 ± 5 nm calculated from the XRD 00l reflections in Fig. 2, using Scherrer's equation.[31] The difference can be attributed to the film strain and the XRD instrumental error. Generally, a surface pyrochlore phase is manifested by small grains of few nanometers in size located at the grain boundaries.[12] These grains are not visible in the SEM, indicating that the pyrochlore phase observed in the XRD pattern is located in the film depth.

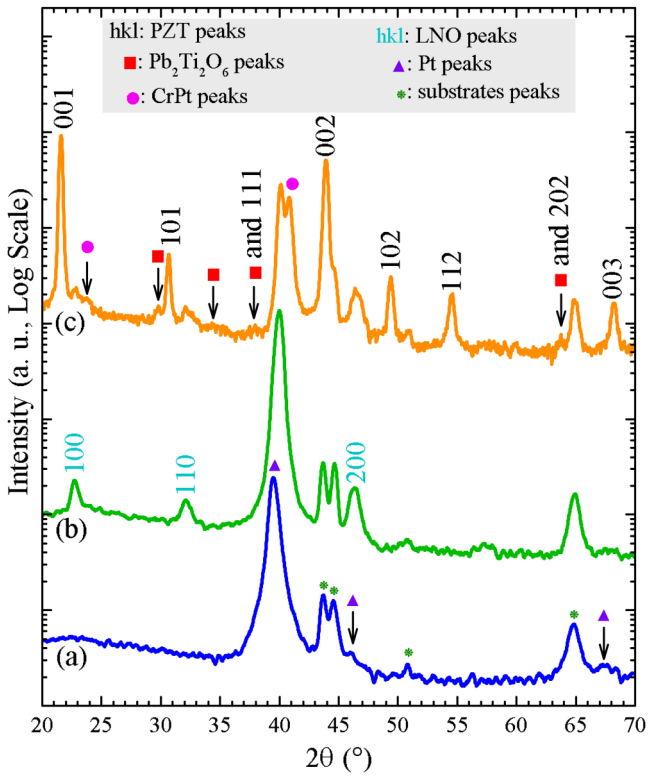

FIG. 2. θ–2θ XRD patterns of (a) an Al_2O_3/Pt/steel sample covered with (b) LNO and (c) PZT layers. The reflections are denoted for the PZT[25] (tetragonal black hkl indexes), LNO[22] (cubic turquoise hkl indexes), Pt[26] (triangles) layers of the heterostructure, as well as for $Pb_2Ti_2O_6$[27] (squares) and CrPt[28] (circles) additional phases. The notation "substrate peaks" (asterisks) corresponds to SS304.[29,30] The Al_2O_3 layer is amorphous.

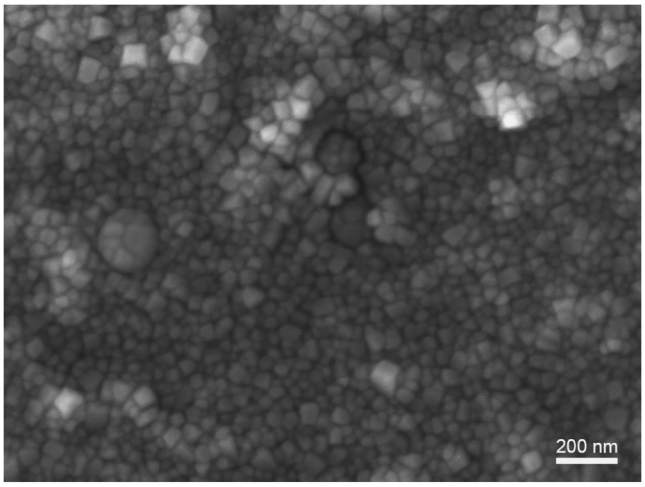

FIG. 3. SEM image of a PZT/LNO/Al_2O_3/Pt/steel sample. The image was taken using a Secondary Electron (SE) mode.

In order to unambiguously measure the texture of the PZT films in spite of the substrate curvature, EBSD measurements were performed. Indeed, the primary electron beam used for the EBSD measurements has much smaller dimensions than the x-ray beam used to record the XRD pattern in Fig. 2. The EBSD analysis of the PZT film texture is performed on a small 3.8 μm by 10 μm area of the sample, for which substrate bending is small and can be neglected.

The pole figure of the PZT film obtained from the EBSD measurements is presented in Fig. 4. The measurement was performed on a sample without Pt top electrodes and sputter-coated with a thin layer of carbon to avoid charging. The highest reflection intensity is indicated in red, while the lower intensities are denoted in blue and green hues. A single reflection can be seen along the {001}-axis, indicating a strong {001} texture of the PZT thin film, which is consistent with the high $f_{PZT} = 0.91$ calculated from the XRD data. This crystallographic orientation in PZT has a large piezoelectric response and is, therefore, preferable for applications.[32,33]

No other reflections can be observed along the {111}- and {110}-axes, indicating no other orientations of the PZT thin films within the resolution limit of the EBSD. For this reason, occurrence of a limited number of grains with orientations other than {001} cannot be excluded in the investigated samples.

The 200 nm and 400 nm thick PZT films show a permittivity of 350 and 349 and a dielectric loss of 4.1% and 2.6% with an instrumental error of 0.15%, respectively.

The low permittivity values can be explained by the predominantly {001} texture of the PZT films, leading to the occurrence of ferroelectric domains with an out-of-plane polarization, referred to as *c*-domains. Indeed, it is established in the literature that *c*-domains permittivity is lower than the one of *a*-domains.[12,14] However, the dielectric permittivity values of the PZT films, obtained at 1 kHz before the *P*–*E* loop measurements, are lower than those of ∼600, ∼780, and ∼790 reported in the literature for 0.6 μm thick Nb-doped PZT films on Ni foils,[14] 1 μm thick PZT films on Ni foils,[12] and 500 nm thick rhombohedral PZT films on ferritic steel deposited by the sol-gel method,[15] respectively. This result is consistent with the fact that Nb-doping enhances domain wall mobility in PZT and increases its permittivity.[14] The presence of pyrochlore in the thin films deposited in this work, even in limited quantities, would also contribute to their lower permittivity.

Nonetheless, the permittivity reported in this work for the {001}-textured PZT thin films is higher than the value of 192 reported in the literature for non-textured films on austenitic stainless steel.[20] Moreover, the dielectric loss of 4.1% and 2.6% in our PZT films is lower than that of 10.2% reported for those films.

Furthermore, the grain size obtained here is relatively small as compared to the values of 63 nm–192 nm reported in the literature for the PZT films grown by PLD on various substrates.[34] Small grain sizes increase the density of both grain boundaries and domain walls and might lower the domain wall mobility, hence

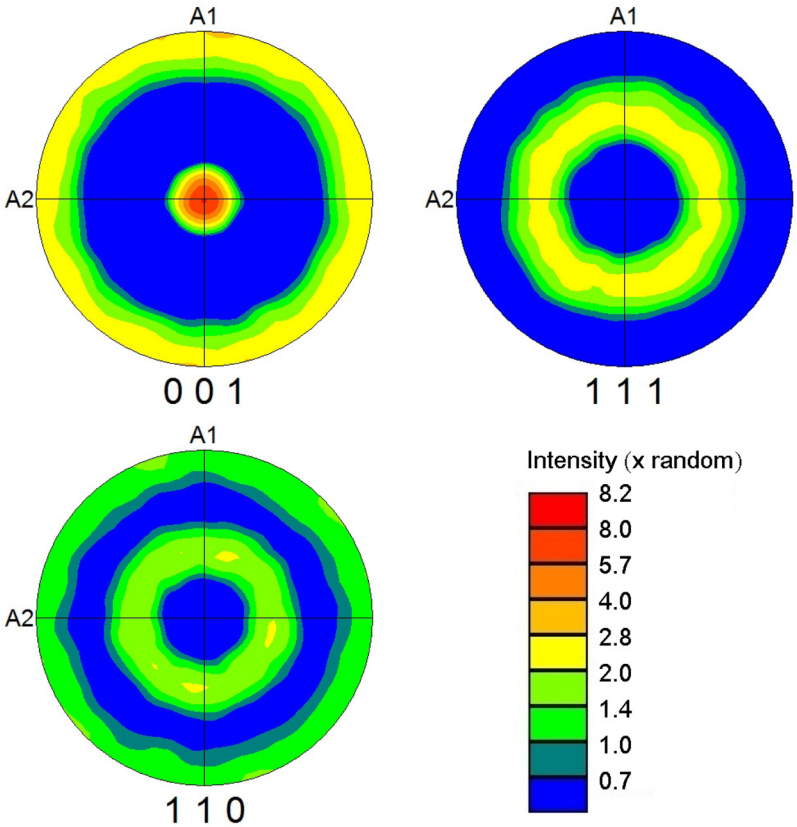

FIG. 4. Pole figure of the PZT layer of a PZT/LNO/Al_2O_3/Pt/steel sample by EBSD. A dataset with more than 7000 indexed grains covering a 3.8 μm by 10 μm area was used to calculate the crystallographic texture using the harmonic series expansion method with a series rank of 24, a Gaussian half width of 5°, and no enforced symmetry. The color scale is logarithmic.

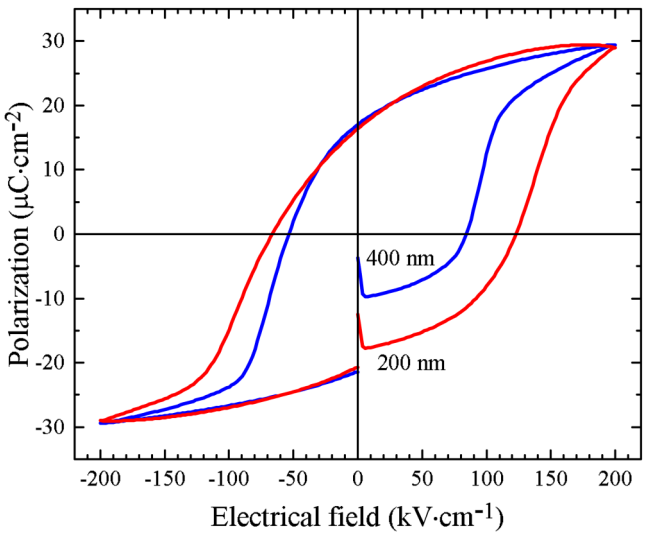

FIG. 5. Polarization vs electrical field hysteresis loops at 100 Hz of 200 nm and 400 nm thick PZT layers of PZT/LNO/Al_2O_3/Pt/steel samples, respectively.

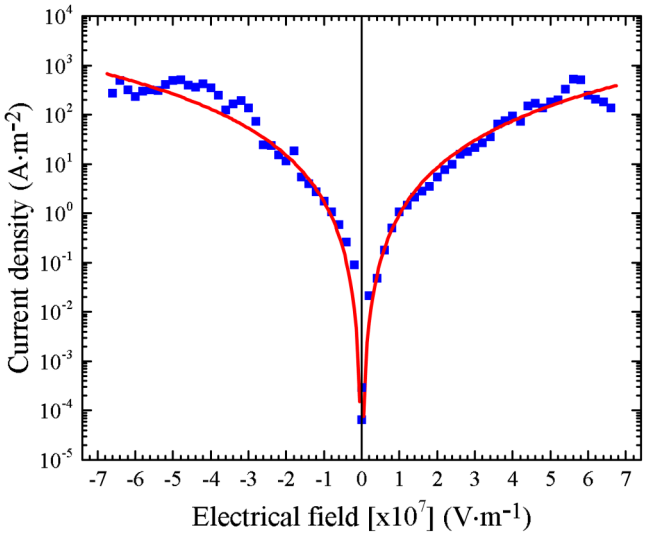

FIG. 6. Leakage current density of the 400 nm thick PZT layer of the PZT/LNO/Al_2O_3/Pt/steel sample (blue squares) fitted within the SCLC scenario with the polynomial function $J \propto E^{3.15}$ for the positive polarity and with the polynomial function $J \propto E^{3.12}$ for the negative polarity (red curves).

limiting ferroelectric properties.[35] The lower permittivity of the produced PZT films might also be due to their reduced thickness[36] as compared to that of about 1 μm, which is usually reported in the literature.[12,14]

The *P*–*E* loops for both samples measured at 200 kV cm^{-1} are presented in Fig. 5. The hysteresis of the 200 nm thick film is larger and more rounded than the one of the 400 nm thick film for which the polarization is nearly saturated. The difference is attributed to larger leakage of the 200 nm thick film due to its reduced thickness.

The *P*–*E* loop of the 200 nm thick sample displays different shapes on its positive and negative branches; there is higher conduction on the upper branch. This phenomenon is less pronounced in the 400 nm thick PZT film due to the lower leakage.

The DC leakage current density of the 400 nm thick PZT sample is plotted in Fig. 6 as a function of the positive and negative applied electric field (*J*–*E* curve). The *J*–*E* curve is fitted with polynomial functions of the electric field $J \propto E^{3.15}$ and $J \propto E^{3.12}$ for the positive and negative polarities, respectively, which are attributed to a space-charge limited current (SCLC) mechanism with trap filling, described by[37,38] $J \propto E^N$ with $N > 2$.

The leakage current density is similar for both polarities. The presence of leakage is coherent with the rounded shape of the *P*–*E* loops in Fig. 5, especially for the 200 nm thick film. While the conduction mechanism in these films is not predominantly interface-driven, the interfaces between the PZT thin film and the electrodes, influenced by the electrode materials, impact on leakage current, particularly on the thinner 200 nm thick film.

Note that the SCLC fit of the *J*–*E* curve in Fig. 6 is not perfect, indicating that other physical mechanisms might contribute in the transfer of the leakage through the PZT film. See the supplementary material for additional information.

The precise values of the coercive fields, E_c, for the 200 nm and 400 nm thick samples were determined from the switching current vs field hysteresis loops as the fields corresponding to the switching current peaks. See the supplementary material for switching current vs field hysteresis loops. The datasets used were the same as their respective *P*–*E* loops plotted in Fig. 5. For the 200 nm thick sample, the positive coercive field at 100 Hz is $E_c = 135.9$ kV cm^{-1} and the internal bias field displayed is 21.0 kV cm^{-1}. For the 400 nm thick sample, the coercive field is $E_c = 93.9$ kV cm^{-1} and the internal bias field is 12.0 kV cm^{-1}.

These coercive fields for PZT thin films are larger than those of ~73 kV cm^{-1} reported in the literature for 1 μm thick PZT films deposited on Ni foils.[12] The internal bias field indicates a preferred polarization direction. For this reason, an external field applied in the opposite direction would result in significant changes in the polarization.[39]

From the *P*–*E* loops in Fig. 5, after the applied electric field of 200 kV cm^{-1} was released, the 200 nm and 400 nm thick PZT films exhibit a remanent polarization, P_{rem}, of $P_{rem} = 16.7\,\mu$C cm^{-2} and $P_{rem} = 16.4\,\mu$C cm^{-2}, respectively.

Thus, both 200 nm and 400 nm thick films show similar remanent polarization and permittivity values. The main difference in behavior between these thin films is the higher leakage in the thinner film, leading to the less saturated *P*–*E* loop.

IV. SUMMARY AND OUTLOOK

Predominantly {001} textured $PbZr_{0.52}Ti_{0.48}O_3$ thin films were grown by PLD onto AISI 304 stainless steel substrates. The combination of Pt, Al_2O_3, and $LaNiO_3$ buffer layers prevents the

oxidation of the steel substrates during the growth of the PZT layer and provides a growth template for its {001} texture.

200 nm and 400 nm thick PZT films show a dielectric permittivity of ~350, a dielectric loss below 5% at 1 kHz, and a remanent polarization of $\sim 16.5\,\mu C\,cm^{-2}$. The saturation of the *P–E* loops and coercive fields is dependent on the film thickness.

In order to understand the applicability of these films, their properties after poling as well as their piezoelectric response still need to be investigated. However, the low dielectric constant and high coercive fields make them suitable for transducer applications. This work, based on stainless steel substrates, is the first step toward transducers with improved fracture toughness relative to Si substrate-based transducers.

SUPPLEMENTARY MATERIAL

See the supplementary material for the SEM image of the cross section of the PZT/LNO/Al_2O_3/Pt/SS304 heterostructure as well as for the switching current vs field hysteresis loops and the fitting of the DC leakage current density.

ACKNOWLEDGMENTS

The authors thank Alexey Arzumanov for performing the Ar ion beam milling of the samples as well as Julian Walker for the discussion on the characterization of samples.

This work was funded by the Deutsche Forschungsgemeinschaft (DFG) under Grant No. AL 560/19-1.

A travel grant from the EIT RawMaterials IDS-FunMat-Inno is also acknowledged.

DATA AVAILABILITY

The data that support the findings of this study are available within the article.

REFERENCES

[1]S. Trolier-McKinstry and P. Muralt, "Thin film piezoelectrics for MEMS," J. Electroceram. **12**, 7–17 (2004).
[2]I. Kanno, "Piezoelectric MEMS: Ferroelectric thin films for MEMS applications," Jpn. J. Appl. Phys. **57**, 040101 (2018).
[3]C.-B. Eom and S. Trolier-McKinstry, "Thin-film piezoelectric MEMS," MRS Bull. **37**, 1007–1017 (2012).
[4]M. D. Nguyen, H. Nazeer, K. Karakaya, S. V. Pham, R. Steenwelle, M. Dekkers, L. Abelmann, D. H. A. Blank, and G. Rijnders, "Characterization of epitaxial Pb(Zr, Ti)O_3 thin films deposited by pulsed laser deposition on silicon cantilevers," J. Microelectromech. Microeng. **20**, 085022 (2010).
[5]S. Dunn and R. W. Whatmore, "Substrate effects on domain structures of PZT 30/70 sol-gel films via PiezoAFM," J. Eur. Ceram. Soc. **22**, 825–833 (2002).
[6]L. Ceresara, A. Iembo, F. Fuso, M. Labardi, M. Allegrini, E. Arimondo, A. Diodati, B. E. Watts, F. Leccabue, and G. Bocelli, "Pulsed laser ablation deposition and characterization of superconductive/ferroelectric bilayers," Supercond. Sci. Technol. **9**, 671–677 (1996).
[7]K. Morimoto, I. Kanno, K. Wasa, and H. Kotera, "High-efficiency piezoelectric energy harvesters of *c*-axis-oriented epitaxial PZT films transferred onto stainless steel cantilevers," Sens. Actuators A **163**, 428–432 (2010).
[8]J.-R. Cheng, W. Zhu, N. Li, and L. E. Cross, "Electrical properties of sol-gel-derived Pb($Zr_{0.52}Ti_{0.48}$)O_3 thin films on a $PbTiO_3$-coated stainless steel substrate," Appl. Phys. Lett. **81**, 4805–4807 (2002).
[9]Q. Zou, H. E. Ruda, B. G. Yacobi, K. Saegusa, and M. Farrell, "Dielectric properties of lead zirconate titanate thin films deposited on metal foils," Appl. Phys. Lett. **77**, 1038–1040 (2000).
[10]Q. Zou, H. E. Ruda, and B. G. Yacobi, "Improved dielectric properties of lead zirconate titanate thin films deposited on metal foils with $LaNiO_3$ buffer layers," Appl. Phys. Lett. **78**, 1282–1284 (2001).
[11]J. H. Yi, R. Seveno, and H. W. Gundel, "Sol-gel derived PZT/RuO_2 multilayer films on stainless steel substrates," Integr. Ferroelectr. **23**, 199–214 (1999).
[12]H. G. Yeo and S. Trolier-McKinstry, "{001} Oriented piezoelectric films prepared by chemical solution deposition on Ni foils," J. Appl. Phys. **116**, 014105 (2014).
[13]T. Xue, H. G. Yeo, S. Trolier-Mckinstry, and S. Roundy, "A wrist-worn rotational energy harvester utilizing magnetically plucked {001} oriented bimorph PZT thin-film beams," in *TRANSDUCERS 2017—19th International Conference on Solid-State Sensors, Actuators and Microsystems* (IEEE, 2017), pp. 375–378.
[14]K. Coleman, J. Walker, T. Beechem, and S. Trolier-Mckinstry, "Effect of stresses on the dielectric and piezoelectric properties of Pb($Zr_{0.52}Ti_{0.48}$)O_3 thin films," J. Appl. Phys. **126**, 034101 (2019).
[15]G. Magagnin, "Chemical solution processed ferroelectric thick films on metal foil," final year internship thesis (Ecole Centrale de Lyon, France—Georgia Tech, USA, 2019).
[16]M. Koinuma, H. Ohmura, Y. Fujioka, Y. Matsumoto, and S. Yamada, "Preparation of PZT thin films on stainless steel using electrochemical reduction," J. Solid State Chem. **136**, 293–297 (1998).
[17]M. Oikawa and K. Toda, "Preparation of Pb(Zr, Ti)O_3 thin films by an electron beam evaporation technique," Appl. Phys. Lett. **29**, 491–492 (1976).
[18]T. Suzuki, I. Kanno, J. J. Loverich, H. Kotera, and K. Wasa, "Characterization of Pb(Zr, Ti)O_3 thin films deposited on stainless steel substrates by RF-magnetron sputtering for MEMS applications," Sens. Actuators A **125**, 382–386 (2006).
[19]T. Nishi, T. Ito, H. Hida, and I. Kanno, "Shoe-mounted vibration energy harvester of PZT piezoelectric thin films on metal foils," J. Phys.: Conf. Ser. **773**, 012062 (2016).
[20]T. Ito, T. Nishi, T. Umegaki, H. Hida, and I. Kanno, "The piezoelectric PZT thin films deposited on metal substrates," J. Phys.: Conf. Ser. **1052**, 012094 (2018).
[21]M. Zhu, P. Komissinskiy, A. Radetinac, M. Vafaee, Z. Wang, and L. Alff, "Effect of composition and strain on the electrical properties of $LaNiO_3$ thin films," Appl. Phys. Lett. **103**, 141902 (2013).
[22]International Centre for Diffraction (ICDD), "Powder Diffraction File (PDF): 04-007-6256," $LaNiO_3$ @ 298 K (2013).
[23]Euro Inox—The European Stainless Steel Development Association, *Stainless Steel: Table of Technical Properties*, 2nd ed., Materials and Applications Series Vol. 5 (Euro Inox, Luxembourg, 2007), p. 16.
[24]F. K. Lotgering, "Topotactical reactions with ferrimagnetic oxides having hexagonal crystal structures—I," J. Inorg. Nucl. Chem. **9**, 113–123 (1959).
[25]International Centre for Diffraction (ICDD), "Powder Diffraction File (PDF): 01-072-7167," Pb($Zr_{0.52}Ti_{0.48}$)O_3 @ 298 K (2013).
[26]International Centre for Diffraction (ICDD), "Powder Diffraction File (PDF): 00-004-0802," Pt @ 298 K (2013).
[27]International Centre for Diffraction (ICDD), "Powder Diffraction File (PDF): 00-026-0142," $Pb_2Ti_2O_6$ @ 298 K (2019).
[28]International Centre for Diffraction (ICDD), "Powder Diffraction File (PDF): 03-065-4629," CrPt @ 298 K (2019).
[29]International Centre for Diffraction (ICDD), "Powder Diffraction File (PDF): 00-033-0397," $Fe_{0.49}Cr_{0.29}Ni_{0.16}C_{0.06}$ @ 298 K (2019).
[30]International Centre for Diffraction (ICDD), "Powder Diffraction File (PDF): 00-034-0396," $Cr_{0.26}Fe_{1.74}$ @ 298 K (2019).
[31]P. Scherrer, "Bestimmung der inneren struktur und der Größe von kolloidteilchen mittels röntgenstrahlen," in *Kolloidchemie Ein Lehrbuch* (Springer, Berlin, 1912), pp. 387–409.
[32]J. Cardoletti, A. Radetinac, D. Thiem, J. Walker, P. Komissinskiy, B. X. Xu, H. Schlaak, S. Trolier-Mckinstry, and L. Alff, "Modelling of the vertical deflection of ferroelectric bending tongues loaded at their free end," AIP Adv. **9**, 025017 (2019).

[33]G. L. Brennecka, W. Huebner, B. A. Tuttle, and P. G. Clem, "Use of stress to produce highly oriented tetragonal lead zirconate titanate (PZT 40/60) thin films and resulting electrical properties," J. Am. Ceram. Soc. **87**, 1459–1465 (2004).
[34]M. D. Nguyen, E. P. Houwman, H. Yuan, B. J. Wylie-Van Eerd, M. Dekkers, G. Koster, J. E. Ten Elshof, and G. Rijnders, "Controlling piezoelectric responses in $Pb(Zr_{0.52}Ti_{0.48})O_3$ films through deposition conditions and nanosheet buffer layers on glass," ACS Appl. Mater. Interfaces **9**, 35947–35957 (2017).
[35]N. Bassiri-Gharb, I. Fujii, E. Hong, S. Trolier-Mckinstry, D. V. Taylor, and D. Damjanovic, "Domain wall contributions to the properties of piezoelectric thin films," J. Electroceram. **19**, 49–67 (2007).
[36]J. Pérez de la Cruz, E. Joanni, P. M. Vilarinho, and A. L. Kholkin, "Thickness effect on the dielectric, ferroelectric, and piezoelectric properties of ferroelectric lead zirconate titanate thin films," J. Appl. Phys. **108**, 114106 (2010).
[37]A. Rose, "Space-charge-limited currents in solids," Phys. Rev. **97**, 1538–1544 (1955).
[38]F.-C. Chiu, "A review on conduction mechanisms in dielectric films," Adv. Mater. Sci. Eng. **2014**, 578168.
[39]J. F. Shepard, F. Chu, I. Kanno, and S. Trolier-McKinstry, "Characterization and aging response of the d_{31} piezoelectric coefficient of lead zirconate titanate thin films," J. Appl. Phys. **85**, 6711–6716 (1999).